arXiv:0807.4615v1 [astro-ph] 29 Jul 2008

Discovery of hot gas in outflow in NGC3379

G. Trinchieri

INAF-Osservatorio Astronomico di Brera, Via Brera 28, 20212 Milano, Italy

ginevra.trinchieri@brera.inaf.it

S. Pellegrini

Dipartimento di Astronomia, Universita di Bologna, Via Ranzani 1, 40127 Bologna, Italy

G. Fabbiano, R. Fu, N. J. Brassington, A. Zezas, D-W. Kim

Harvard-Smithsonian Center for Astrophysics, 60 Garden St., Cambridge, MA 02138

J. Gallagher

Department of Astronomy, University of Wisconsin, Madison, WI 53706-1582

L. Angelini

Laboratory for X-ray Astrophysics, NASA Goddard Space Flight Center, Greenbelt, MD 20771

R. L. Davies

Sub-Department of Astrophysics, University of Oxford, Oxford OX1 3RH, UK

V. Kalogera

Northwestern University, Department of Physics and Astronomy, Evanston, IL 60208

A. R. King

Theoretical Astrophysics Group, University of Leicester, Leicester LE1 7RH, UK

and

S. Zepf

Department of Physics and Astronomy, Michigan State University, East Lansing, MI 48824-2320

ABSTRACT

We report the discovery of a faint ($L_x \sim 4 \pm 1.5 \times 10^{37}$ erg s^{-1}, 0.5-2 keV), out-flowing gaseous hot interstellar medium (ISM) in NGC 3379. This represents the lowest X-ray luminosity ever measured from a hot phase of the ISM in a nearby early type galaxy. The discovery of the hot ISM in a very deep *Chandra* observation was possible thanks to its unique spectral and spatial signatures, which distinguish it from the integrated stellar X-ray emission, responsible for most of the unresolved emission in the *Chandra* data. This hot component is found in a region of $\sim$ 800 pc in radius at the center of the galaxy and has a total mass M$\sim 3\pm1\times10^5$ $M_\odot$. Independent theoretical prediction of the characteristics of an ISM in this galaxy, based on the intrinsic properties of NGC 3379, reproduce well the observed luminosity, temperature, and radial distribution and mass of the hot gas, and indicate that the gas is in an outflowing phase, predicted by models but not observed in any system so far.

Subject headings: X-rays: ISM — galaxies: NGC 3379 — galaxies : elliptical and lenticular — X-rays : galaxies

1. Introduction

The nature of the X-ray emission of elliptical galaxies has been debated since their discovery as X-ray sources with the *Einstein Observatory*, which led to the early suggestion of ubiquitous hot X-ray emitting halos in hydrostatic equilibrium (Forman et al. 1985). These halos would originate from the stellar ejecta resulting from their normal evolution, accumulated during the lifetime of the galaxies, and retained by their deep dark matter potentials. However, from the analysis of these early observations and of ROSAT and ASCA data, a more complex picture of the X-ray emission emerged, suggesting that the non-nuclear X-ray emission of these galaxies consist of varying amounts of hot ISM, and of a baseline component related to the stellar population, either from the finale stages of stellar evolution (i.e. low-mass X-ray binaries, LMXBs, Trinchieri & Fabbiano 1985; Canizares et al. 1987; Kim, Fabbiano & Trinchieri 1992; Fabbiano et al. 2006; Matsushita et al. 1994) or possibly from coronal stellar emission (Pellegrini & Fabbiano 1994). Although controversial at the time, this picture has important implications for the evolutions of the stars and of the gaseous components of ellipticals, suggesting halo retention in the most massive systems, and partial or full winds in most galaxies (Ciotti et al, 1991; David et al. 1991; Pellegrini & Ciotti 1998).

With *Chandra* for the first time the X-ray emission of nearby ellipticals can be imaged, and the existence of the different emission components can be pursued by direct observational means. These observations have led to the detection and study of LMXB populations (see

review in Fabbiano 2006), and the removal of their contamination from the diffuse emission component (e.g. NGC 1316, Kim & Fabbiano 2003). In some galaxies this diffuse emission is due to gaseous halos; however, in other galaxies, where the X-ray luminosity function can be probed to very low luminosities and the residual emission is itself of low luminosity, unresolved LMXBs and possibly stellar emission may account for a large amount or even the bulk of the X-ray luminosity (e.g.NGC821, Pellegrini et al 2007a,b; M32, Revnintsev et al. 2007).

We can now attempt to constrain the presence and properties of vestigial hot halos in these gas-poor galaxies. Since ellipticals are expected to host super-massive nuclear black holes (e.g., Richstone et al. 1998), which are however radiatively quiescent in most cases (Fabian & Canizares 1988, Pellegrini 2005, Ho 2008), these measurements provide useful constraints for models of halo evolution and nuclear feedback (e.g., Springel, Di Matteo & Hernquist 2005; see Pellegrini et al 2007b). The nearby, gas-poor, early-type galaxy NGC3379 provides an excellent target for these investigations. This is a very well studied prototypical elliptical, with $L_B = 1.5 \times 10^{10}$ $L_{B\odot}$. A series of very deep exposures were obtained for this galaxy by our team (PI: Fabbiano), as part of a very large *Chandra* program aimed at unraveling and studying the different X-ray emission components of ellipticals. Together with pre-existent archival data (David et al 2005), these observations resulted in an integrated exposure of 337 ks with ACIS S-3 (see Brassington et al. 2008 for details). In this paper we present our analysis of the diffuse/unresolved X-ray emission component of this galaxy. This analysis leads us to conclude that in addition to the unresolved emission of faint LMXBs and other stellar sources (Revnivtsev et al. 2008), a hot ISM is likely to be present in the central 800 pc of NGC3379.

We discuss our data analysis in Section 2, and our interpretation of these results in Section 3. Our conclusions are summarized in Section 4. We assume a distance of 10.6 Mpc (Tonry et al. 2001), which gives a scale of 51 pc/$''$.

2. Analysis and Results

We have used the same dataset that Brassington et al. (2008) used to determine the source list and compose the most complete X-ray catalog to-date in NGC 3379, down to (0.3-8.0) keV luminosities $L_x \sim 10^{36}$ erg s^{-1}. All sources in the catalog have been excluded from the present analysis. We have used an aperture of $2''$ radius. On axis, this aperture encircles $> 97/95\%$ of the Point Spread Function (PSF), for energies 0.5/1.5 keV (see Figures 4.6 and 4.20, and Table 4.2 in The Chandra Proposers' Observatory Guide, and our own simulations with ChaRT, see Appendix), and it degrades very slowly to encircle $\sim 90\%$ at

$\geq 3'$ for the same energies (Fig. 4.13 in the The Chandra Proposers' Observatory Guide). As will become apparent in what follows, this work will concentrate on the central area NGC 3379, of $\sim 80''$ radius; therefore, our data are not affected by the degradation of the *Chandra* point response function, and we do not need to consider a larger area for source exclusion. We discuss the possible contamination of the PSF in the Appendix.

The size of the area considered also ensures a very homogeneous coverage from all five observations, since the region under study resides well within the area uniformly covered in all the *Chandra* exposures (roughly a $8' \times 5'$ rectangle, see Fig. 1 in Brassington et al. 2008). Therefore we do not need to resort to modelling of the exposure, and we can use a local estimate of the background from the same merged dataset. This procedure minimizes the uncertainties introduced by using a template or "blank sky observations" of different portions of the sky at different times, to estimate the field background.

We have used two different merged datasets for our analysis. All five observations were used for the spatial analysis but only the four most recent observations were merged for the spectral analysis, given the significantly different response of the ACIS S3 CCD in the first observation obtained in 2001 (AO2). Since this observation has the shortest exposure, not using it will not significantly degrade the statistics, while reducing the systematic error from the calibration uncertainties. The responses of the last four observations over the area of interest are virtually identical

2.1. Radial Distributions of the X-ray Surface Brightness

Fig. 1 shows azimuthally averaged radial profiles of the diffuse X-ray emission in the (0.3-2.0 keV) and (2.0-5.0) keV energy bands. The choice of the spectral ranges is motivated by our intention to discriminate between a harder band (2.0-5.0) keV, where all the emission, resolved and unresolved, is likely to arise from stellar sources, and a softer band (0.3-2.0) keV, to which a hot ISM may contribute. We have excluded all detected sources (as explained above), and centered the concentric annuli on the nucleus, identified as the optical/IR center and coinciding with source # 81 in Brassington et al. (2008). Note that as a consequence of this, and also due to source crowding at the center, the X-ray profiles cannot probe the very central region within r=2–3$''$. The raw profiles shown in Fig. 1 flatten at a radius of $> 80''$, indicating that the field background dominates. We can therefore use the $100'' - 140''$ region to estimate the local background and subtract it from the emission, to produce the net profiles shown in Fig. 1-right in the same energy bands. Note that the soft profile is more extended and more centrally peaked relative to the hard profile.

In Fig 2 we divide the full energy range considered in three, and show the azimuthally averaged net profiles in the (0.3-0.7) keV, (0.7-1.5) keV and (1.5-5.0) keV bands. This choice of energy boundaries was motivated by the results of the spectral analysis of the diffuse emission (see next section, Fig 5), to maximize the contribution of the two optically thin thermal plasma component identified in the X-ray spectrum, with temperatures of $\sim$ 0.3 keV and at $\sim$ 1 keV, respectively. It is clear from Fig. 2 that while both the very soft and the harder component follow a similar radial distribution, the soft (0.7-1.5 keV) component has a distinct excess for galactocentric radii r$\leq 20''$.

In the same Fig. 2 we plot the radial profiles in the optical and in the near IR K-band, from the HST F814 filter image and the 2MASS k-band image, obtained from their respective archives (see also Cappellari et al. 2006). These profiles are also azimuthally averaged, but do not cover the full 360° azimuthal plane of the galaxy, except for the very center ($10''$ and $30''$ radius for HST and 2MASS respectively) since the two images only partially cover the galaxy. We also add the Sauron I-band data profile from Cappellari et al. (2006) that cover instead the full extent of the galaxy. The profiles are normalized to the X-ray data by rescaling them for radii r$> 100''$.

With the exception of the very central region ($< 3''$ radius), the optical-IR profiles follow one another, and trace well the distribution of the very soft and hard X-ray profiles. On the contrary, the (0.7-1.5) keV profile is more centrally peaked and only becomes consistent with the shape of the optical-IR ones at r$> 15''$.

2.2. Spectral Analysis

We have analyzed the spectral data extracted in the $2''-15''$, $2''-30''$ and $2''-45''$ regions from the merged dataset from the four more recent observations. Most of the results discussed here come from the $2'' - 30''$ region, which is a reasonable compromise that includes a large fraction of the diffuse emission at high significance, but all regions studied give a consistent picture. To increase the statistical significance of each spectral bin, we have binned the data to obtain a minimum significance of 2σ or better in the net data. The spectral fits are done assuming the line-of-sight galactic N_H of 2.7×10^{20} cm^{-2}, the abundance tables of Wilms et al. (2000), the APEC model to account from the optically thin thermal emission of a plasma, with abundances fixed at the 100% value (different values do not change the final results), and a Bremsstrahlung to account for the X-ray emission of unresolved fainter LMXBs and stellar X-ray sources.

We find that a single APEC component, with kT$\sim$0.3 keV, and a 7 keV Bremsstrahlung

model are able to approximate the data and give an acceptable value for the reduced $\chi^2 \sim 1$. However, inspection of the residuals shows a noticeable excess at around 1 keV (with a peak at about 5 σ) and a less significant deficit at 0.6-0.8 keV, as shown in Fig. 3. The addition of a second APEC component reduces the χ^2 value and most of all eliminates the excess, suggesting two separate components at 0.3 keV and 1.0 keV (Fig. 3, bottom). Fig. 4 shows the 68%, 90% and 99% confidence regions for the two interesting parameters, the temperatures of the very soft and soft components. Fig. 5 shows the best-fit unfolded spectral components, from which it becomes evident that the ~ 1 keV component is clearly dominant over the ~ 0.3 keV component in the 0.7-1.5 keV band.

We tested whether the existing data support a requirement of a second soft plasma component in the spectrum, by computing the Bayesian Information Criterion (BIC), discussed by Schwarz (1978; an astronomical introduction to it can be found in Liddle 2004, and an application in Tajer et al. 2007) for both models. This quantity approximates the Bayes factor (Jeffreys 1961; Kass & Raftery 1995), which gives the posterior odds of one model against another, presuming that the models are equally favored prior to the data fitting (Liddle 2004). The difference ΔBIC can be used to evaluate the relative value of the two models. We find ΔBIC of 5-6 (depending on the region used), which can be used as a strong evidence (see Jeffreys 1961; Liddle 2004) that we are justified in introducing the 1 keV component in the spectral modelling.

We have investigated further the spatial distribution of the different spectral components by comparing the spectra from the $2'' - 15''$ and $20'' - 30''$ regions, both fitted with a single APEC spectrum at 0.3 keV (Fig. 6). It is clear that there is no residual emission at 1 keV in the spectrum from the outer region; this suggests that the additional "soft" component is more concentrated towards the center, consistent with the radial profile comparison of Fig. 2.

From the spectral results we can estimate the luminosity of each individual component, summarized in Table 1. The measured unabsorbed luminosity of the total unresolved emission, within the $30''$ region, is $\mathrm{L_x} \sim 4 \pm 0.4 \times 10^{38}$ erg s^{-1} in the 0.3-10 keV range, equally divided below and above 2 kev. The hard band luminosity is totally accounted for by the Bremsstrahlung component, which alone gives a luminosity $\mathrm{L}_x \sim 1 \pm 0.1 \times 10^{38}$ erg s^{-1} in the 0.5-2.0 keV band. The 1 keV component contributes for $\mathrm{L_x} \sim 4^{+2.5}_{-0.2} \times 10^{37}$ erg s^{-1} in this band, and the residual $\mathrm{L_x} \sim 6^{+2.5}_{-0.4} \times 10^{37}$ erg s^{-1} is due to the 0.3 keV emission. Errors are estimated from the best fit values (68% confidence values, from XSPEC). We have estimated a correction factor to recover the area lost due to masking the point sources (see Table 1), and a second one to account for the fraction of emission not included in the area used in the spectral analysis (given in Table 2). These can be used to estimate the total luminosity

of the very soft and hard components, which we list in Table 2. The component at 1 keV appears to contribute only in the central region, for r $< 30''$.

3. Summary of results and comparison with the literature

We have analyzed the spectral and spatial distribution of the diffuse X-ray emission in NGC 3379 with deep *Chandra* data, cleaned of all detected sources down to a threshold luminosity $L_x \sim 10^{36}$ erg s^{-1} (see Brassington et al. 2008). The residual emission can be detected only out to r $\sim 1'$, corresponding to 3 kpc, well within the D_{25}, measured at $5.4' \times 4.8'$ (from NED, see also Cappellari et al. 2006).

The spectral distribution of this unresolved emission in the $30''$ region used for the spectral analysis suggests the presence of 3 distinct components. The dominant contribution in the broad 0.3-10 keV band can be modeled with a Bremsstrahlung emission at ~ 7 keV and is likely to arise from lower luminosity LMXBs and other stellar components that can not be detected individually in the present data, as also suggested by its spatial distribution, which follows that of the optical and IR stellar light (Fig. 2). This component accounts for all of the emission above 2 keV and about 1/2 of the emission below 2 keV, and has an estimated total $L_x \sim 5 \times 10^{38}$ erg s^{-1} (0.5-10 keV, see Table 2).

We also find two additional optically thin thermal components, with best fit temperatures of ~ 0.3 keV and ~ 1 keV, contributing roughly 2/3 and 1/3 of the 0.5-2.0 keV residual luminosity, respectively (see Table 1), in the $30''$ radius region. This result is supported by the combined evidence of excess emission at ~ 1 keV over the dominant 0.3 kev plasma in the spectral data (Fig. 3), and of a different spatial distribution of the two components, when the data below and above 0.7 keV are selected (Fig. 2).

On average, the 0.3 keV component has a spatial distribution consistent with that of the lower luminosity LMXBs and coronally active stars (traced by the emission above 1.5 keV) and of the stars (traced by the I-band and K-band emission), while the 1 keV emission is more centrally peaked, and is prominent out to r $\sim 15'' - 20''$.

Two previous detailed studies of the diffuse emission of NGC 3379 based on *Chandra* data can be found in the literature. Based on the first 2001 short observation David et al. (2005) conclude that the diffuse emission is dominated by undetected faint point sources, but with a 10% contribution from a gaseous component, with kT$\sim$ 0.6 keV, in the central 770 pc. This hot ISM would have a luminosity of $\sim 9 \times 10^{37}$ erg s^{-1}(0.3-10 keV) and a mass of $\sim 5 \times 10^5$ $M_\odot$. Our estimate of the luminosity of the optically thin thermal diffuse emission in the same region is consistent with that of David et al (2005), but we are able

to distinguish two separate components of this emission. NGC 3379 is also included in the sample examined by Fukazawa et al. (2006), who also report a detection of a component at 0.5 keV in a small region of the galaxy.

More recently, Revnivtsev et al. (2008) have suggested a different interpretation for the unresolved emission: using the full dataset as in the present work, they derive a radial profile of the 0.5-2.0 keV emission, cleaned of detected sources, which they compare with the K-band profile. Based on this comparison they conclude that all of the unresolved emission observed in NGC 3379 can be attributed to the emission of stellar sources, with no evidence of a truly diffuse ISM. Our net radial profile of Fig. 1 is entirely consistent with that of Revnivtsev et al. (2008), giving us confidence that slight differences in the data analysis, in the subtraction of detected sources obtained with different algorithms or in the choice of the background level, are not significant sources of discrepancies. The main difference between this work and Revnivtsev et al. (2008) therefore lies in our spectral and spatial analysis, that enables us to distinguish two separate spectral components of the soft diffuse emission, with different spatial properties, which contribute equal amounts to the total in the inner 15″ radius.

4. Discussion

Our analysis suggests the presence of three components of the diffuse emission of NGC 3379. As summarized above, the hard and very soft emission are spatially consistent with a stellar origin; a detailed discussion of this integrated X-ray emission from stellar sources (LMXBs, cataclysmic variables, active stars and stellar coronae) is given by Revnivtsev et al (2008). This stellar emission has been invoked to explain the diffuse X-ray emission of the Galactic Ridge (Revnivtsev et al 2006, Sazonov et al. 2006), the bulge of M31 (Bogdán & Gilfanov 2008), M32 (Revnivtsev et al. 2007) and NGC821 (Pellegrini et al 2007a).

In what follows we will concentrate on the emission of the (0.7-1.5) keV band. This component has a different spatial distribution, more concentrated in the center and more centrally peaked than the stellar emission (see Fig. 2), indicating a different origin. We suggest that this component is likely to originate from a ∼1 keV hot plasma, and discuss it in the context of an appropriate model for a galactic flow.

4.1. Evidence for hot ISM in NGC 3379

The interpretation of the 0.7-1.5 keV emission detected in NGC 3379 as due to a different component than the softer and harder ones opens the possibility that this is the long sought for evidence of a hot ISM in this galaxy (e.g., Ciotti et al. 1991, David et al. 2005). However, as shown by Fig. 5, all three components contribute to the 0.7-1.5 keV emission, while both the softer, and in particular the harder, energy ranges are less contaminated by the other components. The spectral results can be reliably used to estimate the contribution of each component to the total luminosity. To estimate the spatial distribution of each separately, we have to resort to a few reasonable assumptions, which we have already discussed and that we summarize below: a) the profiles in both the very soft and hard energy bands are very similar in shape, therefore we can treat them as having a common origin with different rescaling factors; b) they are also consistent with the I-band and K- band profiles, again with possibly different rescaling along the full spatial extent probed; and c) the 0.7-1.5 keV profile is also consistent in shape with all above profiles for r$>15''$, where there is no longer any evidence of the emission due to the 1 keV component (Fig. 6). We can therefore reasonably conclude that the 0.7-1.5 keV emission at r$>15''$ traces the soft and hard components, and that an extrapolation at smaller radii could be used to give a reasonable estimate of the local contribution from the stellar component at different radii. We have used the K-band data normalized to the 0.7-1.5 keV emission at r$>15''$ as the best proxy to extrapolate the profile at smaller radii, since we can use it as a model with virtually no errors. While this relies on the assumption that the stellar light is a good tracer of the X-ray binary population, with no local, though small, variations, the observed agreement with the X-ray profiles of the residual emission at softer and harder bands (Fig. 2) supports this assumption. We therefore derive the radial distribution of the $\sim$ 1 keV component as the excess over our model (Fig. 7) which we can now compare to the expected emission from a hot ISM, derived from the hydrodynamical simulations described below. Note that the X-ray luminosity derived from integrating the radial distribution of Fig. 7 is $L_x \sim 2.5 \pm 1 \times 10^{37}$ erg s^{-1}, consistent with that derived from the spectral analysis.

From the spectral results and the assumption of spherical symmetry, we can estimate the average density and total mass of gas responsible for the emission measured. We derive a very low density of $n_e \sim 0.007$ cm^{-3} and a total mass of gas M$\sim 3 \times 10^5$ M$_\odot$, in a region of $\sim$ 770 pc in radius at the center.

4.2. The hot gas from hydrodynamical simulations

The round optical shape (morphological type E1), its optical colors, typical of an old population (Terlevich & Forbes 2002), and the lack of signs of current or past interactions (Schweizer & Seitzer 1992) allow us to assume that a simple "passively evolving" stellar population feeds a hot gas flow, whose evolution can be reasonably studied with spherically symmetric hydrodynamical simulations. The numerical code used to solve the time-dependent equations of hydrodynamics with source terms is described in details in Ciotti et al. (1991). We adopt a central grid spacing of 20 pc, which provides a good match to the scale of the observations in the inner regions; the simulations do not cover feedback effects and the flow evolution close to the central massive black hole (Shapiro et al. 2006).

Given the high quality data available for this galaxy, it is possible to build a mass model tailored specifically onto NGC 3379, and consider the best recipes available for the mass and energy source terms. These are briefly described below.

4.3. The mass model

The optical profile is well described by a de Vaucouleurs (1948) law over a span of 10 magnitudes (Capaccioli et al. 1990; Peletier et al. 1990), therefore the simulations use the stellar mass density profile given by the Hernquist (1990) distribution, that is a very good approximation of the de Vaucouleurs law and has the advantage that its dynamical properties can be expressed analytically. We also impose the observed B-band luminosity of 1.5×10^{10} $L_{B\odot}$, the central stellar velocity dispersion of 230 km s^{-1} (from the detailed modeling of ground-based and *HST* spectroscopy, Shapiro et al. 2006) and a total stellar mass $M_* = 10^{11} M_\odot$, obtained from dynamical and stellar population synthesis studies (Saglia, Bertin & Stiavelli 1992, Gerhard et al. 2001, Napolitano et al. 2005, Cappellari et al. 2006, Douglas et al. 2007). The resulting shape of the stellar profile, when projected, is close to the optical profiles in Fig. 2.

The radial density distribution of the dark haloes of ellipticals is not well constrained by observations; theoretical arguments and high resolution numerical simulations of dissipationless collapse produce a density distribution $\propto r^{-1}$ near the center (Dubinsky & Carlberg 1991, Navarro, Frenk, & White 1996). The model galaxy is therefore a superposition of two Hernquist density distributions, one for the luminous matter and one for the dark matter.

The total amount of mass in NGC 3379 has been calculated several times using the observed stellar velocity dispersion profile, extending out to $\sim 1-2$ effective radii (R_e, e.g., Saglia, Bertin & Stiavelli 1992, Kronawitter et al. 2000, Samurovic & Danziger 2005), and

dynamical tracers as planetary nebulae or globular clusters extending out to larger radii (Romanowsky et al. 2003, Dekel et al. 2005, Teodorescu et al. 2005; Pierce et al. 2006, Bergond et al. 2006, Douglas et al. 2007, De Lorenzi et al. 2008). Regardless of the details of the modelling, studies based on the observed stellar velocity dispersion profile invariably show very little dark matter within $R_{\rm e}$, or even no dark matter. Within 2–3 $R_{\rm e}$, the stellar component alone satisfies reasonably well the observations, and the amount of dark matter is constrained to be at most very modest (with a dark to stellar mass ratio of the order of $M_h/M_* \sim 0.1$, Kronawitter et al. 2000; Cappellari et al. 2006). The evidence for dark matter is at the largest scales (10–40 kpc), probed mostly by globular clusters (see also the analysis of an HI ring, Schneider 1985), with a global galactic value of $M_h/M_* = 1.1 - 1.5$ (Dekel et al. 2005), $M_h/M_* \sim 2$ (Puzia et al. 2004), up to $M_h/M_* \sim 6$ (Bergond et al. 2006).

In order to make the model mass distribution consistent with the observations, we also imposed the ratio $M_h/M_* = 0.1$ within one $R_{\rm e}$[1], while on the global galactic scale it has been varied instead between 1 and 6.

4.4. Time evolving inputs

The model does not assume a steady state configuration, therefore the input ingredients of the numerical simulations, which are the rates of stellar mass loss from the aging stellar population and the rate of SNIa heating, are both evolving with time. In the numerical code the exact mass return rate prescribed by the stellar evolution theory is used (Ciotti et al. 1991), updated to take into account the latest stellar population synthesis models and more recent estimates for the mass ejection from stars as a function of their mass (Maraston 2005). This gives a present epoch ($\sim$ 10 Gyr) mass return rate of $\sim 0.3 M_\odot$ yr^{-1} for the whole galaxy.

The SNIa heating rate is parameterized as $L_{SN}(t) = E_{SN}\, R_{SN}(t)\, L_B$, where E_{SN} is the kinetic energy injected in the ISM by one SNIa, and the number of events as a function of time is $R_{SN}(t) L_B \propto t^{-s}$, where the slope s describes the unknown decay rate. $R_{SN}(t)$ is normalized to give the present SNIa's explosion rate in nearby E/S0s of Cappellaro et al. (1999), i.e., $0.16 h_{70}^2$ SNu (where 1 SNu = 1 SNIa per 100 yrs per $10^{10} L_{B,\odot}$, $h_{70} = H_\circ/70$), that has an associated uncertainty of $\sim 30\%$. A detailed theoretical modeling of the evolution of

[1]In the code the presence of dark matter contributes also to produce the observed central stellar velocity dispersion, as described in Pellegrini & Ciotti (2006), though this aspect is not very important here given the small amount of dark matter in the central regions.

the rate shows that, after the first 0.5–1 Gyr, it is well approximated by a power law with a slope $s \sim 1.0 - 1.2$ for double degenerates exploders, and a slope $s \sim 1.5 - 1.7$ for the single degenerate exploders (Greggio 2005).

The thermalization of the stellar mass losses to the local "temperature" set by the stellar velocity dispersion is another heating source, though of lower relevance. Its contribution is determined at each radius using the velocity dispersion profile obtained by solving the Jeans equation for the two-component Hernquist model in the globally isotropic case (Pellegrini & Ciotti 2006). For realistic anisotropy distributions, the difference with the isotropic case is small; in addition, the heating due to thermalization of stellar motions is significantly smaller than SNIa heating.

4.5. Results and comparison with observations

With the SNIa's explosion rate from Cappellaro et al. (1999) and the adopted mass model, the resulting gas flow phase is of a global outflow, with velocities ranging from 10^7 to a few 10^7 cm s^{-1}, going from the central region to the galaxy outskirts (e.g., subsonic out to r$\sim$1 kpc and supersonic outwards). When varying the total amount of dark matter within the range $M_h/M_* = 1-6$ allowed for by observations, this flow pattern keeps basically the same (provided that the SNIa's rate increases together with M_h/M_*, but still within its observational uncertainty).

For the resulting gas flows, the X-ray luminosity in the energy bands of 0.3–2 keV and 2–8 keV, and the temperature weighted with the emission in the 0.3–8 keV band ($< kT >$), have been calculated. In order to do this, the values of the cooling function $\Lambda(T, Z)$, as a function of temperature, have been obtained with the APEC code in XSPEC, for solar abundance, consistent with the estimate for the stellar population (Terlevich & Forbes 2002); a "best fit" Λ was then derived from these values and used in the L_X and $< kT >$ calculation (that takes into account the whole density and temperature distributions over the computational grid).

After $\sim$ 9 Gyr, the gas has a 0.3–2 keV luminosity of 2×10^{37} erg s^{-1}, in good agreement with the observed one. This is a reasonable time scale that corresponds to the estimated age of NGC 3379: Terlevich & Forbes (2002) give an age of $9.0^{+2.3}_{-1.9}$ Gyr; more recently, a mean age in the range 8–15 Gyr has been confirmed by Gregg et al. (2004) and Denicolò et al. (2005). The central temperature is $\sim 10^7$ K out to a few hundred pc, and is steeply declining outwards; the central gas density is $n_e = 2 \times 10^{-2}$ cm^{-3} and is also steeply declining outwards. The mass of the hot gas is $\sim 3 - 4 \times 10^5 M_\odot$ within a radius of 800 pc (in good

agreement with that obtained in Sect. 4.1). The emission weighted gas temperature within a radius of 15″ is $< kT >\sim 0.8$ keV, a value near the lower range of those allowed for by observations (see Fig. 4). The projection along the line of sight of the 0.3–2 keV emission is shown in Fig. 7, for two models with a total $M_h/M_* = 4$, a SNIa's rate close to that of Cappellaro et al. (1999), and a slope for the SNIa's decay rate of $s = 1.0$ and $s = 1.5$. Both model profiles reproduce well the observed "gas profile" derived above. We note that a larger age for the gas flow would result in a lower stellar mass loss rate and lower gas content, with consequently lower ISM emission, below the observed one.

5. Conclusions

With the very deep *Chandra* observation of NGC 3379 we have scored two firsts: we have the first evidence of a very small amount of hot ISM in a nearby galaxy, down to the level of $L_x \sim 4 \times 10^{37}$ erg s^{-1} (0.5-2.0 keV), and at the same time we have the first evidence that this gas is in an outflow phase, which has been predicted by models but as of yet has not been observed. As a third and equally important result, we find that detailed modelling based on the optical data (stellar mass, total mass and supernova rate) reproduces remarkably well the observed total luminosity, total mass and spatial distribution of the hot phase of the gas.

After detection and removal of point sources down to a luminosity of $L_x \sim 10^{36}$ erg s^{-1} we have been able to study the unresolved emission in NGC 3379. The detailed spectral analysis has led us to the evidence of three separate components: a very soft (plasma at kT$\sim$0.3 keV) and a hard (Bremsstrahlung at kT=7 keV) components can be attributed to the integrated emission of unresolved sources, closely linked to the stellar population (binary systems and coronally active stars, as discussed by Revnivtsev et al. 2008). However we also detect a hot ISM in this galaxy, within the innermost $\sim$ 800 pc, with a luminosity $L_x \sim 4 \pm 1.5 \times 10^{37}$ erg s^{-1} (0.5-2.0 keV). This is lowest detection of a hot gas in a nearby early-type galaxy. The total gas mass involved is also very small, of a few 10^5 $M_\odot$.

With the aid of hydrodynamical simulations and a galaxy model tailored specifically on NGC3379, we have reproduced both the luminosity and the average radial distribution of this hot gas component. For a SNIa's explosion rate consistent with current estimates, the gas is outflowing, even for the "maximum" dark matter model, where the amount of dark mass is the maximum allowed for by optical studies.

6. Appendix: Consideration upon the effects of the PSF

.

At the suggestion of the referee, we have thoroughly checked that the results obtained above, in particular the detection of the ~ 1 keV component, are not due to a faulty subtraction of the detected sources. We have run several tests, which we illustrate below.

1) We have first redone the spatial and spectral analysis assuming a circle of 2.5" and 3" radius for point source exclusion, with analogous results, albeith somewhat larger errors, due to the smaller statistics available.

2) We have also simulated the *Chandra*'s PSF using ChaRT (Carter et al. 2003). Since we were interested in the wings of the PSF, we have run several simulations for 20,000 counts each and then merged the resulting images to increase the statistics at radii larger than $1''$ We have used the average spectrum obtained in the inner $15''$, inclusive of all detected sources, as an input parameter in all simulations. We have then treated the results as we have the data of NGC 3379, namely we have produced radial profiles in the same energy bands and calculated the expected contribution from point sources in the regions of interest. We expect that 4% of the counts detected from a point sources within $2''$ from its peak falls in the $2'' - 30''$ region, and 3.6% in the $2'' - 15''$ region, in the 0.3-2.0 keV band (with values between 3% and 5% in the softer and harder of the bands considered). If we integrate the contribution due to the "wings" of all point sources detected in a radius=$30''$, we can only account for 10-25% of the detected counts in the 0.3-0.7, and 0.7-1.5 keV bands in the unresolved component. This is a generous estimate of the contribution from the discrete population, since only sources at the center of the region will contribute the full amount, the wings of the others being only partially included in the region considered.

3) We have used the current documents online[2] and directly contacted the experts on both the PSF and its wings (Dr. T Gaetz and D. Jerius) to better understand the effects of the wings of the point spread function. The most updated studies on the PSF wings are based on the ground XRCF and on-orbit Her X-1 data. Both data sets demonstrate the existence of the PSF wings, but the effects of this component decrease rapidly with decreasing energy. The ray trace model used to simulate the PSF (point 2 above) includes some of the effects of wings, and appears to be reliable at low energies (< 2 keV) and small radii, although it might be underestimating the wing effects at energies above 2.0-2.5 keV. However, we are mostly interested in the emission below ~ 1.5 keV and relatively small radii, where the model appears to be adequate.

[2] `http://cxc.harvard.edu/cal/Hrma/psf/index.html`

4) We have re-analyzed the spectrum of the emission in the $2'' - 15''$ regions excluding only the 5 brightest sources with a significantly smaller exclusion region of $1''$ radius. This exclusion is necessary to avoid that the point source population completely dominates the spectral results; on the other hand, if the sources were responsible for the 1 keV component, it should be significantly stronger when sources are included in the spectral analysis. The spectral results indicate that, while the net counts increase by a factor of 4, the 1 keV component only increases by a factor of 1.5 the original value, consistent with the ratio of the areas of the regions considered.

All in all, we believe that the excess emission observed in the 0.7-1.5 keV band is a real effect, and is not an artifact related to the wings of the many individual sources detected in the area. This excess is relative to the emission in adjacent energy bands, and is seen at energies where the effects of PSF wings are significantly smaller than at higher energies. We also believe that there is excess emission over the scattering from the detected point sources, although we are fully aware of the fact that the exact evaluation of its strength has large uncertainties, both in the soft and in particular in the hard band.

We thank Stefano Andreon for many interesting discussion on the statistical aspects of the data analysis, and Terry Gaetz and Diab Jerius for their help in understanding the PSF issues. We thank the referee for raising the issue of the effects of the PSF, that prompted us to better investigate the reliability of the results. The data analysis was supported by the CXC CIAO software and CALDB, and has made use of the SAOImage DS9 and funtools softwares, developed by the Smithsonian Astrophysical Observatory. We have used the NASA NED and ADS facilities, and have extracted archival data from the *Chandra*, HST and 2MASS archives. This work was supported by the *Chandra* GO grant G06-7079A (PI: Fabbiano) and sub-contract G06-7079B (PI: Kalogera). We acknowledge partial support from NASA contract NAS8-39073 (CXC); A. Zezas acknowledges support from NASA LTSA grant NAG5-13056; S. Pellegrini acknowledges partial financial support from the Italian Space Agency ASI (Agenzia Spaziale Italiana) through grant ASI-INAF I/023/05/0.

Facilities: CXO (ACIS).

REFERENCES

Bergond, G., Zepf, S. E., Romanowsky, A. J., Sharples, R. M., & Rhode, K. L. 2006, A&A, 448, 155

Brassington, N. J. et al 2008, ApJ, submitted.

Bogdan, A., & Gilfanov, M. 2008, ArXiv e-prints, 803, arXiv:0803.0063

Canizares, C. R., Fabbiano, G., & Trinchieri, G. 1987, ApJ, 312, 503

Capaccioli, M., Held, E.V., Lorenz, H., Vietri, M. 1990, AJ 99, 1813

Cappellari, M., Bacon, R., Bureau, M., et al. 2006, MNRAS 366, 1126

Cappellaro, E., Evans, R., Turatto, M. 1999, A&A 351, 459

Carter, C. Karovska, M., Jerius, D., Glotfelty, K., & Beikman, S. 2003, Astronomical Data Analysis Software and Systems XII, 295, 477

Ciotti, L., D'Ercole, A., Pellegrini, S., & Renzini, A. 1991, ApJ, 376, 380

David, L. P., Forman, W., & Jones, C. 1991, ApJ, 380, 39

David, L. P., Jones, C., Forman, W., & Murray, S. S. 2005, ApJ, 635, 1053

Dekel, A., Stoehr, F., Mamon, G. A., Cox, T. J., Novak, G. S., Primack, J. R. 2005, Nature 437, 707

De Lorenzi, F.; Gerhard, O.; Coccato, L. et al. 2008, arXiv:0804.3350

de Vaucouleurs G., 1948, Ann.Ap., 11, 247

Denicoló, G., Terlevich, R., Terlevich, E., Forbes, D. A., & Terlevich, A. 2005, MNRAS, 358, 813

Douglas, N. G., et al. 2007, ApJ, 664, 257

Dubinski, J., Carlberg, R. G. 1991, ApJ 378, 496

Fabbiano, G., et al. 2006, ApJ, 650, 879

2006, ARA&A, 44, 323

Fabian, A.C., & Canizares, C.R. 1988, Nature, 333, 829

Forman, W., Jones, C., & Tucker, W. 1985, ApJ, 293, 102

Fukazawa, Y., Botoya-Nonesa, J. G., Pu, J., Ohto, A., & Kawano, N. 2006, ApJ, 636, 698

Gerhard O., Kronawitter, A., Saglia, R. P., Bender, R. 2001, AJ 121, 1936

Gregg, M. D., Ferguson, H. C., Minniti, D., Tanvir, N., & Catchpole, R. 2004, AJ, 127, 1441

Greggio, L., 2005, A&A 441, 1055

Hernquist L.E., 1990, ApJ, 536, 359

Ho, L.C. 2008, arXiv:0803.2268

Jeffreys H., 1961, Theory of probability, 3rd edn, Oxford Univ. Press, Oxford

Kass R. E., Raftery A. E. , 1995, Journ. American Stat. Assoc., 90, 773

Kim, D.-W., & Fabbiano, G. 2003, ApJ, 586, 826

Kim, D.-W., et al. 2006, ApJ, 652, 1090

Kim, D.-W., Fabbiano, G., & Trinchieri, G. 1992, ApJ, 393, 134

Kronawitter A., Saglia R.P., Gerhard O., Bender R., 2000, A&AS, 144, 53

Liddle, A. R. 2004, MNRAS, 351, L49

Maraston, C. 2005, MNRAS 362, 799

Matsushita, K., et al. 1994, ApJ, 436, L41

Napolitano, N. R., et al. 2005, MNRAS, 357, 691

Navarro, J.F., Frenk, C.S., White, S.D. M. 1996, ApJ 462, 563

Peletier R.F., Davies, R.L., Illingworth, G., Davis, L.E., Cawson, M. 1990, AJ 100, 1091

Pellegrini, S. 2005, ApJ, 624, 155

Pellegrini, S., Ciotti, L. 1998, A&A, 333, 433

Pellegrini, S., Ciotti, L., 2006, MNRAS 370, 1797

Pellegrini, S., Siemiginowska, A., Fabbiano, G., Elvis, M., Greenhill, L., Soria, R., Baldi, A., & Kim, D. W. 2007a, ApJ, 667, 749

Pellegrini, S., Baldi, A., Kim, D. W., Fabbiano, G., Soria, R., Siemiginowska, A., & Elvis, M. 2007b, ApJ, 667, 731

Pellegrini, S., & Fabbiano, G. 1994, ApJ, 429, 105

Pierce, M., Beasley, M. A., Forbes, D. A., et al. 2006, MNRAS 366, 1253

Puzia, T. H., et al. 2004, A&A, 415, 123

Revnivtsev, M., Sazonov, S., Gilfanov, M., Churazov, E., & Sunyaev, R. 2006, A&A, 452, 169

Revnivtsev, M., Churazov, E., Sazonov, S., Forman, W., & Jones, C. 2007, A&A, 473, 783

Revnivtsev, M., Churazov, E., Sazonov, S., Forman, W., & Jones, C. 2008, ArXiv e-prints, 804, arXiv:0804.0319

Richstone, D.; Ajhar, E. A.; Bender, R.; Bower, G.; Dressler, A.; Faber, S. M.; Filippenko, A. V.; Gebhardt, K.; Green, R.; Ho, L. C.; Kormendy, J.; Lauer, T. R.; Magorrian, J.; Tremaine, S. 1998 Nature 395 14

Romanowsky, A. J., Douglas, N. G., Arnaboldi, M., et al. 2003, Science 301, 1696

Saglia R.P., Bertin G., Stiavelli M., 1992, ApJ, 384, 433

Samurovic, S.; Danziger, I. J. 2005, MNRAS 363, 769

Sazonov, S., Revnivtsev, M., Gilfanov, M., Churazov, E., & Sunyaev, R. 2006, A&A, 450, 117

Schneider, S. 1985, ApJ, 288, L33

Schweizer, F., Seitzer, P. 1992, AJ 104, 1039

Schwarz G., 1978, Annals of Statistics, 5, 461

Shapiro, K. L., Cappellari, M., de Zeeuw, T., McDermid, R. M., Gebhardt, K., van den Bosch, R. C. E., & Statler, T. S. 2006, MNRAS, 370, 559

Springel, V., Di Matteo, T., Hernquist, L. 2005, ApJ 620, L79

Tajer, M., et al. 2007, A&A, 467, 73

Teodorescu, A. M., Mendez, R. H., Saglia, R. P., Riffeser, A., Kudritzki, R.-P., Gerhard, O. E., Kleyna, J. 2005, ApJ 635, 290

Terlevich, A. I., Forbes, D.A. 2002, MNRAS 330, 547

Tonry, J.L., Dressler, A., Blakeslee, J.P., et al. 2001, ApJ 546, 681

Trinchieri, G., & Fabbiano, G. 1985, ApJ, 296, 447

Wilms, J., Allen, A., & McCray, R. 2000, ApJ, 542, 914

This preprint was prepared with the AAS LaTeX macros v5.2.

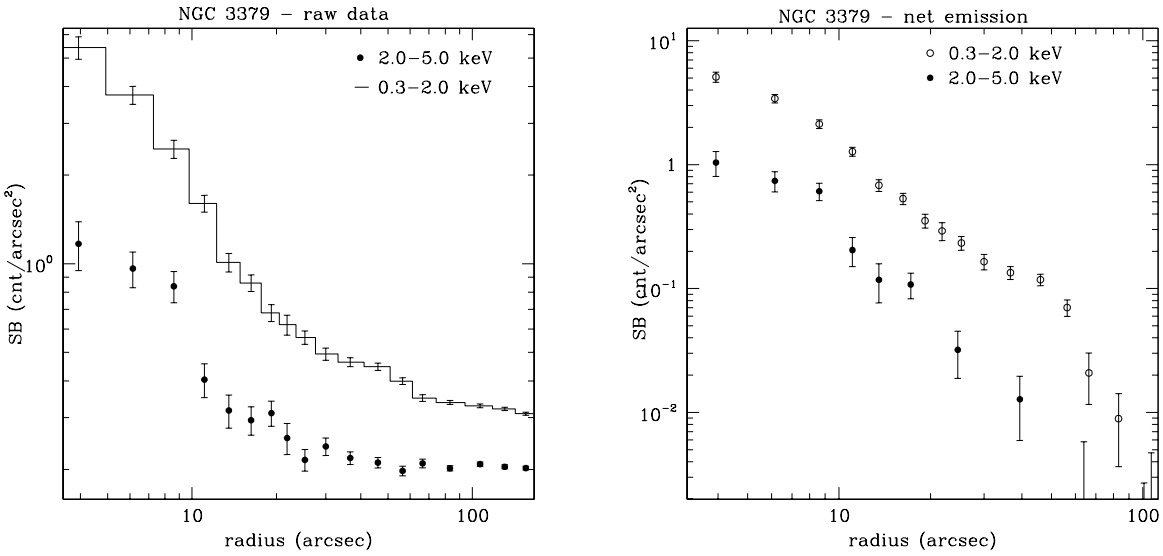

Fig. 1.— Azimuthally averaged radial profiles of the unresolved emission in NGC 3379, in two broad energy bands. Left: raw data; right: background subtracted data

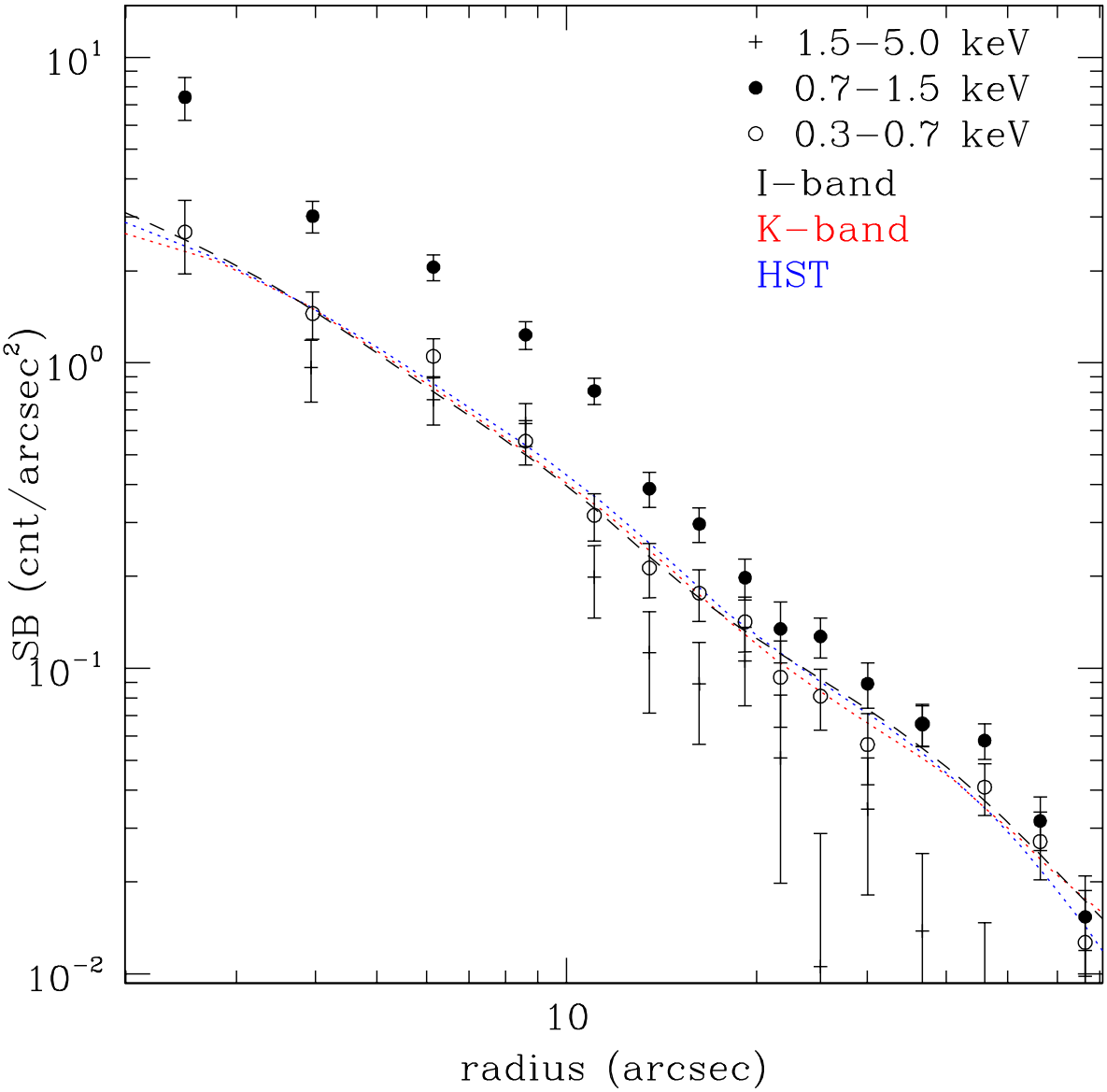

Fig. 2.— Azimuthally averaged net profile in different X-ray bands, compared to the optical and K-band profiles

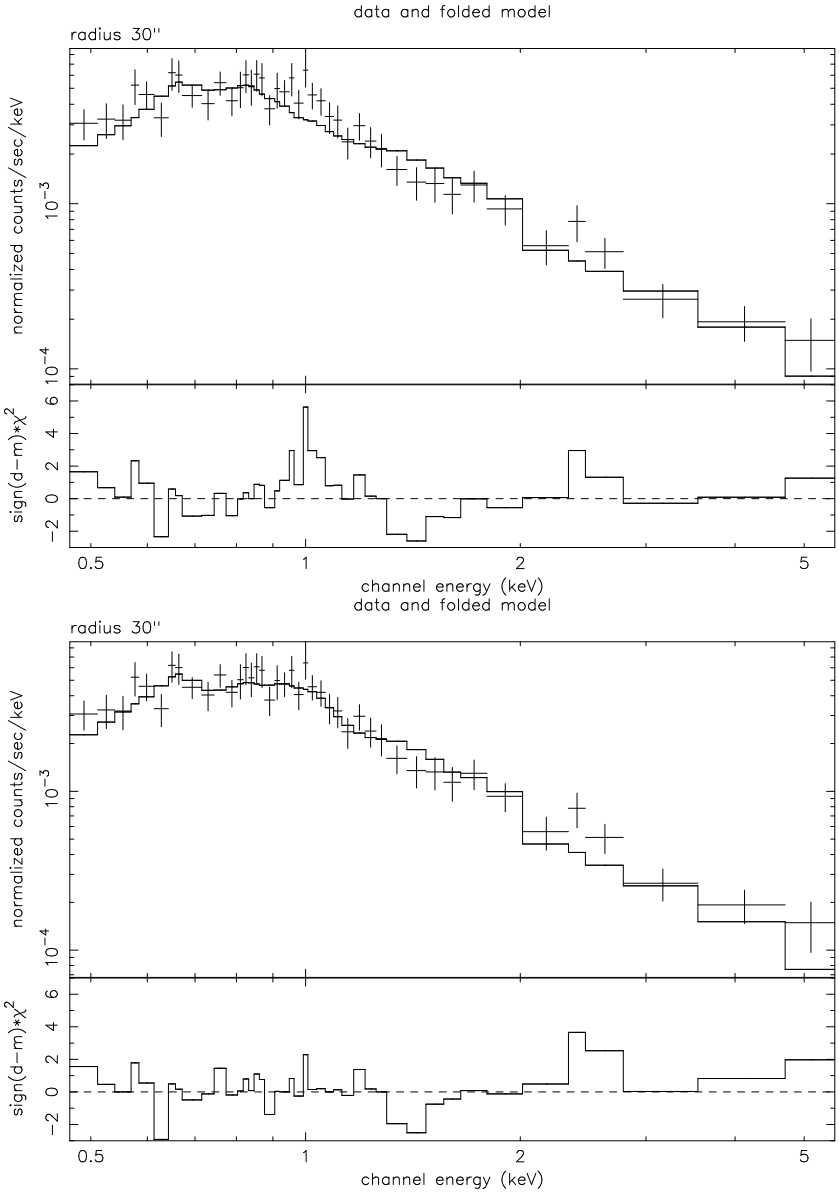

Fig. 3.— Spectral data in the 30″ region, fitted with a single temperature (0.3 keV) and a two temperature APEC model (top and bottom respectively, see text), plus a 7 keV bremsstrahlung. For displaying purposes, data are rebinned to 5σ.

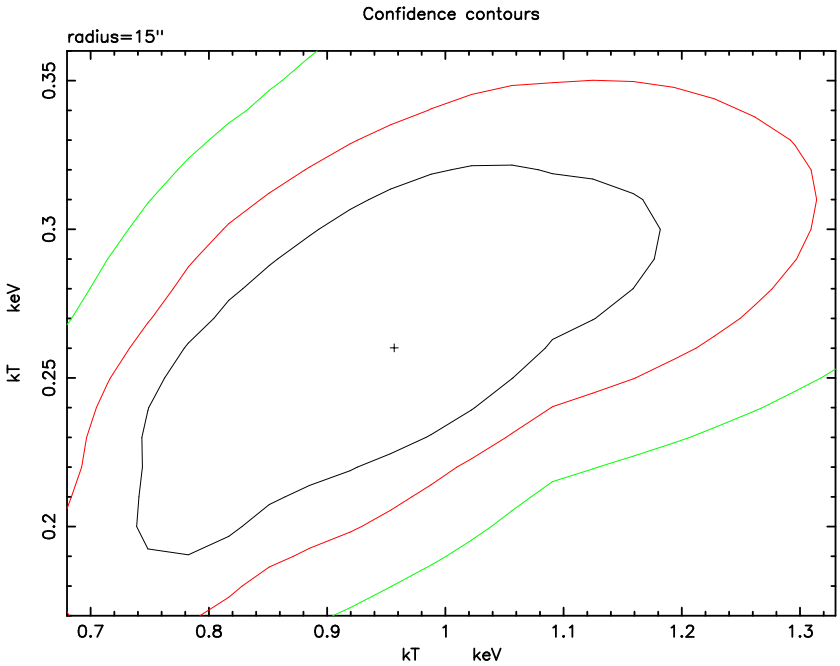

Fig. 4.— Confidence contour regions (at 68, 90 99% level for two interesting parameters) for the two temperatures of the APEC component (see text).

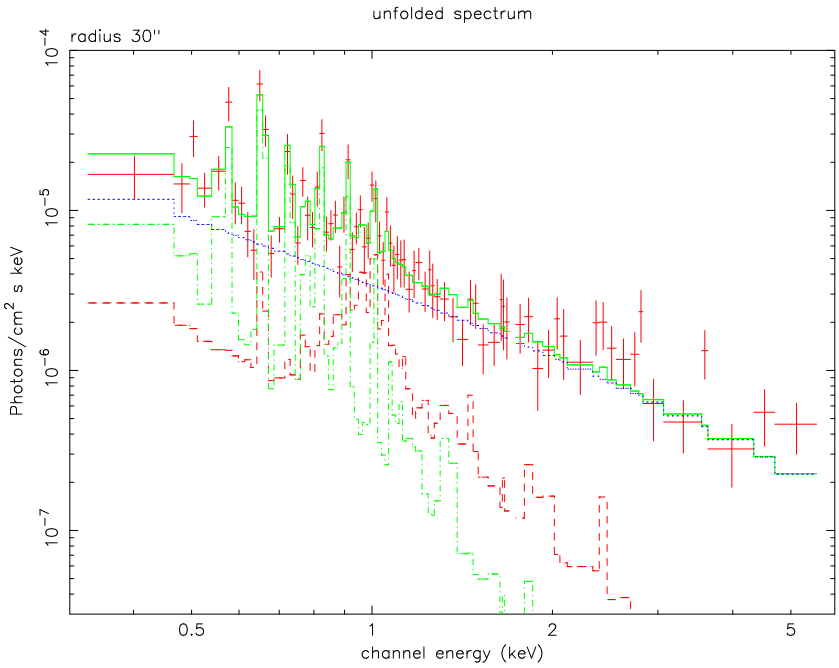

Fig. 5.— Region 30″, unfolded spectrum: 0.3 + 1.0 keV APEC + 7 keV Bremsstrahlung, line-of-sight absorption.

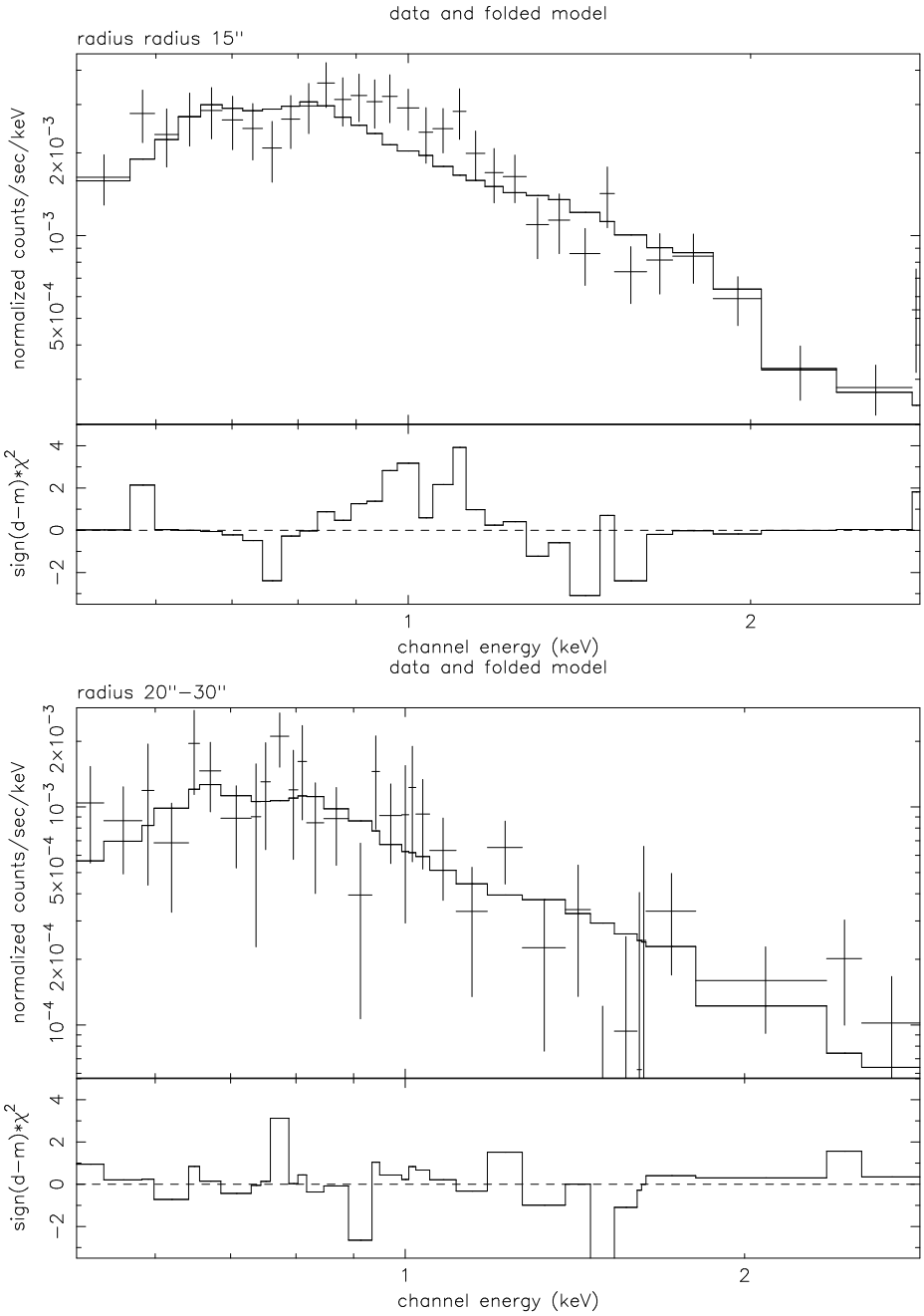

Fig. 6.— Spectral data in the 0″-15″ and 20″-30″ region, fitted with a single temperature plasma model

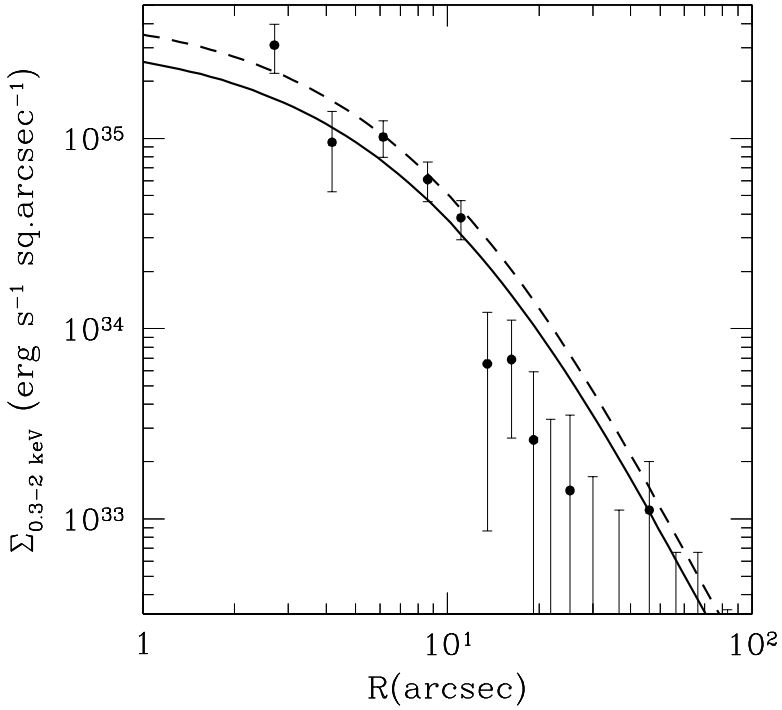

Fig. 7.— The observed 0.3–2 keV emission from the "pure" 1 keV component, compared with the profiles resulting for two gas models, one with $s = 1.0$ (dashed line) and the other with $s = 1.5$ (solid line). See Sect. 4 for more details.

Table 1: Measured luminosities of the different components

Region	Net counts[a]	L_X[b] 0.3-10 keV	L_X[b] 0.5-2.0 keV	L_X[b] 2.0-10.0 keV	B/A1/A2[c] 0.5-2.0 keV	Correction[d]
2″-30″	1550±53	4.4×10^{38}	2.0×10^{38}	2.0×10^{38}	1/0.6/0.35	1.15
2″-15″	978±35	2.9×10^{38}	1.3×10^{38}	1.3×10^{38}	0.8/0.27/0.28	1.34

[a]Net counts used in the spectral fit

[b]Total luminosity in the given band in erg s^{-1}

[c]L_x in the 0.5-2 keV band for the Bremsstrahlung / APEC @ 0.3 keV/ APEC @ 1 keV components, in units of 10^{38} erg s^{-1}

[d]Correction factor to take into account the area lost due to the excised sources

Table 2: Total luminosities of the different components, after correcting for area lost and total extent

Component	Extension (arcsec)	Correction[a]	L_X 0.5-2.0	L_X 2-10
Very soft (0.3 keV)	95	1.60	1.1×10^{38}	2.3×10^{35}
Soft (1 keV)	20	1.00	4.0×10^{37}	5.0×10^{36}
Hard (7 keV)	50	1.35	1.6×10^{38}	3.0×10^{38}

[a]Correction factor to extrapolate from the spectral extraction region (30″, see Tab. 1) to the total source counts